Astronomical Techniques and Instruments, Vol. 2, November 2025, 348–357

Article Open Access

RASI: the Robotic All-Sky narrowband Imager

Yuxin Xin[1,2,3*], Baoli Lun[1,2,3*], Zejun Hu[4,5*], Yue Zhong[1,2], Kai Ye[1,2,3], Hongying Xu[1,2], Yufeng Fan[1,2,3], Bin Li[4,5], Dehong Huang[4,5]

[1]*Yunnan Observatories*, *Chinese Academy of Sciences*, *Kunming* 650216, *China*

[2]*University of Chinese Academy of Sciences*, *Beijing* 100049, *China*

[3]*Key Laboratory for the Structure and Evolution of Celestial Objects*, *Chinese Academy of Sciences*, *Kunming* 650216, *China*

[4]*Center for Space Physics and Astronomy*, *Polar Research Institute of China*, *Shanghai* 200136, *China*

[5]*Arctic Yellow River Earth System National Observation and Research Station*, *Polar Research Institute of China*, *Shanghai* 200136, *China*

*Correspondences: xyx@ynao.ac.cn; lunbl@ynao.ac.cn; huzejun@pric.org.cn

Received: June 30, 2025; Accepted: September 10, 2025; Published Online: September 11, 2025; https://doi.org/10.3724/ati2025054; https://cstr.cn/32083.14.ati2025054

© 2025 Editorial Office of Astronomical Techniques and Instruments, Yunnan Observatories, Chinese Academy of Sciences. This is an open access article under the CC BY 4.0 license (http://creativecommons.org/licenses/by/4.0/)

Citation: Xin, Y. X., Lun, B. L., Hu, Z. J., et al. 2025. RASI: the Robotic All-Sky narrowband Imager. *Astronomical Techniques and Instruments*, **2**(6): 348−357. https://doi.org/10.3724/ati2025054.

Abstract: We report a new standalone Robotic All-Sky narrowband Imager (RASI) for auroral and airglow studies. RASI has new optics and an electromechanical system, low operation and installation costs, easy deployment and fully automatic features. The new optics provide an all-sky field of view with excellent image quality and sensitivity. The new electromechanical system design offers a more compact size and the capability for outdoor independent deployment. We have also developed a fully automatic data acquisition software for RASI, which is based on the perception of solar altitude and the all-sky cloud cover. In conclusion, the RASI demonstrates significant advantages over the traditional all-sky narrowband imager, and it is highly suitable for the intensity measurements of large-scale auroras and airglow distributions.

Keywords: Robotic; All-sky imager; Auroras; Airglow; Optical imaging

1. INTRODUCTION

The Earth's ionosphere (ranging from mesosphere to thermosphere, with an altitude of 60 to 1000 km) serves as an interaction region between Earth's atmosphere and solar radiation (mainly ultraviolet and X-rays). It is rich in free electrons and ions and is the region where auroras and airglow occur. The study of atmospheric and astronomical phenomena benefits greatly from continuous, wide-field imaging of the night sky. All-Sky Imagers (ASI) have become essential tools for observing transient events such as auroras and airglow.

The auroras are created by interactions of air molecules with the solar wind[1,2]. The purpose of the ASI's measurement of auroras is to conduct studies on geomagnetic storms and geomagnetic substorms[3–9]. Airglow (nightglow and dayglow), the faint glow of the atmosphere, is caused by the self-illumination of the upper atmosphere via chemiluminescence processes. The nightglow (also called "Nocturnal airglow") results from the photoionization of atmospheric gases by ultraviolet (UV) sunlight[10]. It has been shown that airglow emissions are altered by gravity waves passing through certain layers of the atmosphere, making it possible to study atmospheric gravity waves (AGWs) and their sources through airglow imaging[11–16]. The ASI can also detect aircraft lights and contrails, satellites, meteors, local light polluters, atmospheric extinction, and transient astronomical objects[17,18]. Furthermore, auroras and airglows, along with starlight and the zodiacal light, all contribute to the brightness of the nonlunar night. As airglows can even outshine scattered moonlight in the near-infrared band, the understanding of the Earth's night-sky brightness requires good knowledge of the complex airglow emission spectrum and its variability[19].

Traditional broadband ASI provides valuable data on spatial and temporal variations in sky emissions[20–23] but lacks the spectral resolution needed to isolate specific chemical species or physical processes. Auroras and airglow emissions occur both as distinct bands (Table 1) and as continuum emission, spanning UV, visible, and near-infrared

Table 1. Radiation spectral lines and radiation sources of the ionosphere

	Excited particles	Color	Wavelength/Å	Altitude/km
Aurora	N_2^+	Blue	3914 4278	90–120
	[OI]	Green Red	5577 6300	90–150 200–400
	[OI]	Near-infrared	7774 8446	200–400 90–150
Airglow	[OI]	Green Red	5577 6300	90–100 200–300
	[OI]	NIR	7774	150–300
	O_2		7620	85–100
	O_2		8446	85–100
	OH		8650	80–100
Sodium layer	[NaI]	Yellow	5890 5896	90

wavelengths. The auroras and night sky spectras[1] are recorded by the Arizona Airglow Experiment during the flight of STS-53, December 1992. Narrowband imaging enables targeted observations of emission lines, which are critical for studying mesospheric and thermospheric dynamics[24–27].

Recent advancements in optical system optimization and automated data processing have significantly improved the efficiency of night-sky monitoring[28–31]. However, most existing ASIs are limited to remote control observation mode, and the installation method is still depends on the rooftops of astronomical observatories or private homes[9, 32–35]. To address this gap, we have developed a standalone Robotic All-Sky narrowband Imager (RASI), which is designed for autonomous, high-resolution spectral imaging with minimal maintenance, and standalone running without a rooftop. The RASI employs a fixed single-filter or multi-filter design, optimized for optical system and electromechanical system, coupled with a high-sensitivity Electron Multiplying Charged-Coupled Devices (EMCCD) or a Scientific Complementary Metal-Oxide-Semiconductor Transistor (sCMOS) detector, and an automatic unattended software control system. It is perfectly suitable for multi-point networked monitoring projects of auroras or airglows emissions, such as: the Mid-latitude All-sky-imaging Network for Geophysical Observations (MANGO) network[9], Time History of Events and Macroscale Interactions During Substorms (THEMIS) ground-based network[32], Super Dual Auroral Radar Network (SuperDARN) [34], and so on.

This paper presents the design, key technology, and initial results of RASI. Section 2 describes the instrument's basic specification parameters, including two different versions: RASI-1 and RASI-2. Section 3 details the instrument's optical system, mechanical-electrical design, and fully automated software architecture. Section 4 discusses preliminary observations, demonstrating the system's ability to resolve fine structures in airglow and aurora layers. Finally, we summarize the article and outline the future application prospects of the two versions of RASI.

2. THE OVERVIEW OF THE RASI

RASI is based on the classic imager design influenced by Mende et al.[36], Hu et al.[37] and Bhatt et al.[9], and including some traditional structures: fisheye lens, telecentric imaging lens, narrowband filter, imaging lens, and camera. However, RASI has some new features in the following aspects: a more integrated and efficient optical design, a new electromechanical design that enables low-cost, independent, and rapid deployment, and a software system capable of achieving intelligent and autonomous observation and operation.

We developed two versions of RASI (RASI-1 and RASI-2, Fig. 1) to meet the requirements of various application scenarios. The main specifications of them are presented in Table 2.

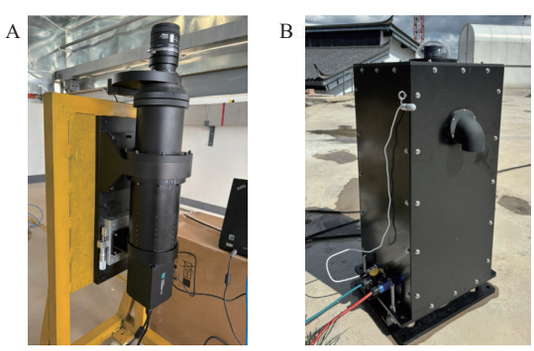


Fig. 1. RASI-1 (A) is a romote control version which need a dome, RASI-2 (B) is a standalone robotic version.

The RASI-1 has an electric narrowband filter wheel with five positions, but RASI-2 employs a filter slot in which a narrowband filter can be manually inserted. Their focuses are both performed manually. The version of RASI-2 is built as a standalone robotic system with a waterproof compact metal frame and an acrylic transparent hemispherical cover with anti-condensation and anti-frosting functions. By using the all-sky cloud cover data provided by the external all-sky near-infrared cloud sensor[21], RASI-2 can autonomously determine and conduct scientific observations based on weather conditions. While RASI-1 can only be installed inside a room or a dome, and conduct scientific observations via remote mode. The universal camera interface design enables RASI to be capable of installing different types of cameras (sCMOS or EMCCD).

The RASI with sCMOS camera is more suitable for observing the auroras and airglows in middle and low latitudes, and the RASI with EMCCD camera is more suitable for observing the auroras and airglows in high lati-

1. *http://glo.lpl.arizona.edu/glo/spectra.html*

Table 2. Specifications of RASI-1 and RASI-2

Items	Specifications	
	RASI-1	RASI-2
Field of view/(°)	180	180
Fisheye lens	Nikon 16 mm F2.8	
Camera type	sCMOS	EMCCD
Camera model	Dhyana 400BSI	Andor iXon888
Camera cooling/(°)	−45	−80
Pixel size/um	6.5	13
Resolution	2048 × 2048	1024 × 1024
Bits depth/bits	16	16
Dark current/(e− pixel^{-1} s^{-1})	0.5	0.0005
Exposure time/s	4	4
Shuttle	Electronic	Mechanical
Filter size	2-inch	2-inch
Filter wheel	Yes	No
Bandwidth/nm	2.5	2.5
Focusing	Manual	Manual
Wavelength coverage/nm	350−900	
Operating temperature/(°)	[−40, 40]	
Operating altitude/m	⩽ 4000	
Operating environment	Indoor	Outdoor
Operating mode	Remote	Robotic

tudes. Because all CCD sensors exhibit blooming and streaking artifacts when the charge in a pixel exceeds the saturation limit, but CMOS not. And the moon (the largest illuminated target in the night sky) has a lower altitude in high-latitude regions. The blooming effect will cause pollution to the normal auroras and auroral glow areas, as shown in Fig. 2.

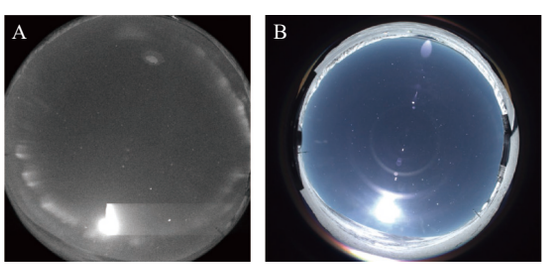


Fig. 2. RASI-2 narrowband gray image (A) and all-sky camera color image (B) at the same time (local time: 2024−11−20 02:08:00) and at Longyearbyen Station.

3. THE SYSTEM DESIGN OF THE RASI

3.1. Optical System

The optical structure of the monochromatic ASI is much more complex than that of the color ASI. Since the radiation spectral lines of the Earth's ionosphere are all sharp and independent, it is necessary to conduct narrowband measurements to effectively eliminate the influence of radiation from other bands.

Fig.3 shows the transmittance curve of the narrowband filter with a bandwidth of 2.5 nm that is selected for the RASIs. If the filter is placed directly near the focal plane of the fisheye camera lens, the bandwidth of the different field positions after passing through the filter will be different. In order to solve this problem, a pair of plano-convex lenses are added in front of the focal plane, to transform the original optical path into an equidistant and telecentric optical path. As shown in Fig. 4, most of the light enters the narrowband filter perpendicularly, except at the 90° position. It basically ensures the consistency of a 2.5 nm bandwidth within a 180° field of view.

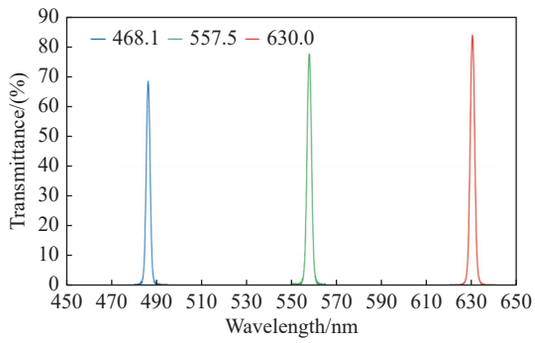


Fig. 3. The transmittance of the narrowband filters.

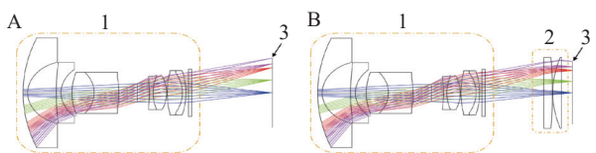


Fig. 4. The optical path of the fisheye lens (A) is transformed into an equidistant and telecentric optical path (B). Different colors represent the incident light from different zenith distance, ranges from 0° to 90° (blue: 0°, green: 30°, red: 60°, pink: 70°, purple: 90°) by adding a pair of plano-convex lenses (1: Fisheye lens; 2: A pair of plano-convex lenses; 3: Narrowband filter).

We have also redesigned the secondary imaging system (SIS, No. 4 in Fig. 5) of the RASI instrument, which is completely different from the traditional ASI.

Firstly, due to the mismatch between the focal plane area of the fisheye lens and the target area of the camera (the plano-convex lenses added at the front merely change the angle of the incident light beam, but do not alter the size of the focal plane), the SIS should have focal reducer function to reduce the imaging area. According to the Equation (1) of an ideal optical system, image height h is in direct proportion to focal length f and field of view θ:

$$h = f\tan\theta \ . \tag{1}$$

Another advantage of the optical system after focal reducer is that it improves the system's sensitivity to weak signals, as the optics are much faster. For RASI, the theoretical detection sensitivity is expected to increase by 3.1 times due to the f-ratio change.

Secondly, the SIS also has the function to correct the aberration caused by the front optical system. Finally, the SIS also includes the imaging function, and the RASI no

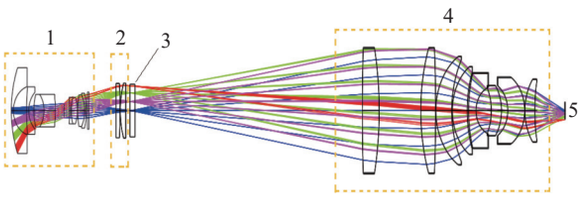


Fig. 5. Schematic of lenses and ray-paths of the RASI optics (1–3: The same as defined in Fig. 4; 4: SIS; 5: Camera).

longer requires a second commercial lens like the traditional ASI does.

The Modulation Transfer Function (MTF) curves of RASI for two observation bands (557.7 nm and 630 nm) are illustrated in Fig. 6, the cut-off frequency is about 38 lp/mm. The Fig. 7 shows their spot diagrams, the Root Mean Square (RMS) spot size for the worst case of image quality is concentrated within 3 to 4 pixels, which is excellent for observation of auroras and airglow.

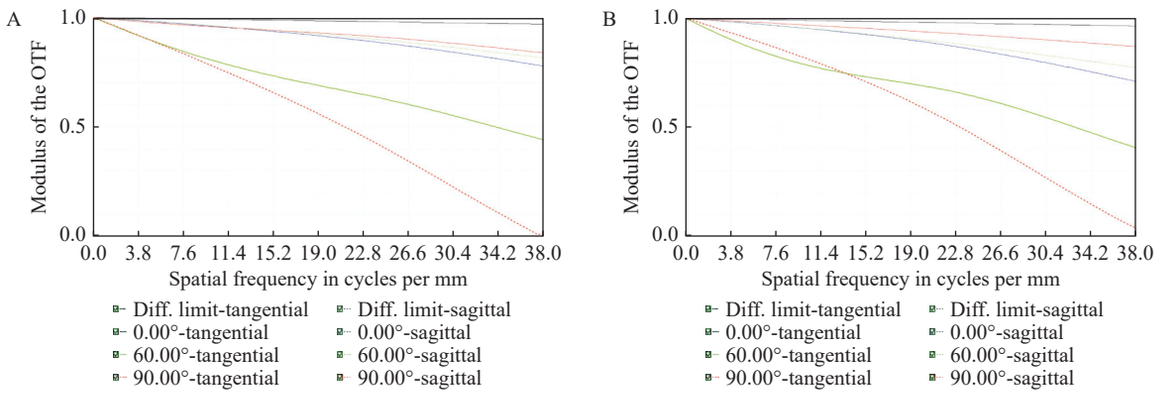


Fig. 6. MTF curves of RASI at the center wavelengths of 557.7 nm (A) and 630 nm (B) within a 2.5 nm bandwidth.

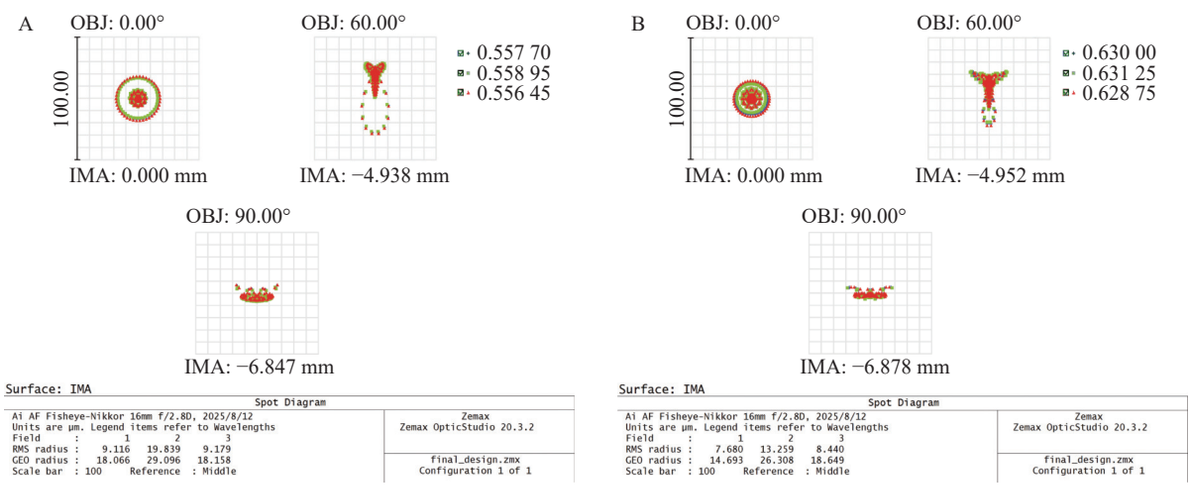


Fig. 7. Spot diagrams of RASI at the center wavelengths of 557.7 nm (A) and 630 nm (B) within a 2.5 nm bandwidth.

In summary, RASI owns a more efficient and compact optical design, and its detection sensitivity and optical quality are both superior to those of traditional ASI.

3.2. Electromechanical System

An obvious limitation of the traditional ASI system with sealed enclosure is frequent condensation during winter months due to the temperature differential between outside and inside the enclosure[9]. Through the innovative design of the electromechanical system of RASI (Fig. 8), the condensation has been effectively eliminated.

The version of RASI-2 is built as a standalone robotic system with a waterproof and thermal-insulated metal frame housing, whose sealing cover plate is made of lightweight and durable bakelite material to reduce its weight (as shown in Fig. 1). At the top of the frame, a semi-spherical transparent cover installation interface plate with a sealing ring is designed, making the installation and replacement of acrylic covers very convenient. At the bottom of the frame, a mechanical structure was designed that can adjust the tilt angle of the equipment. There are also four waterproof and low-temperature resistant plugs, which are used to connect power supply, network connection, external environmental temperature/humidity sensor and the all-sky cloud cover sensor.

A wide temperature industrial personal computer (IPC) is installed inside the frame. The operating system is Linux, and the programming languages are C++ and

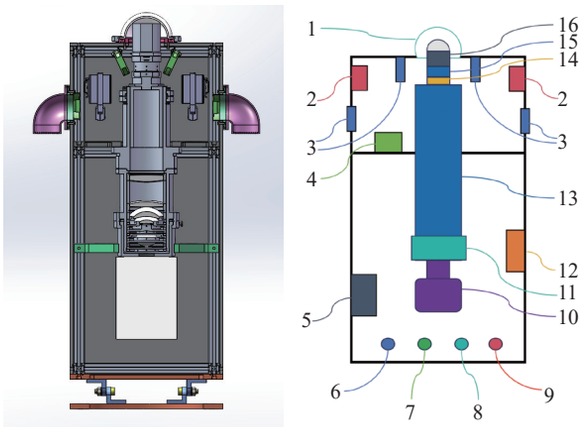


Fig. 8. Mechanical and electrical system structure diagram of the RASI-2 (1: The acrylic transparent protective cover; 2: PTC heaters; 3: Cooling fans; 4: Temperature controller; 5: Mini IPC; 6: Cloud cover sensor cable; 7: Environmental temperature/humidity sensor cable; 8: RJ45 network cable; 9: AC220V power supply; 10: Camera; 11: Focusing mechanism; 12: Low-voltage power supply; 13: SIS; 14: Narrowband filter; 15: Plano-convex lenses; 16: Fisheye lens).

Python. The IPC is responsible for collecting various types of data and for the intelligent control of the camera. Based on the real-time collection of temperature/humidity data inside and outside the metal frame, and through the auto-control of the heater and the cooling fan, the acrylic protective cover has achieved the functions of avoiding condensation in a high-temperature environment and anti-frosting in a low-temperature environment. Through the robustness test of the RASI system under wide temperature conditions in the high and low temperature chambers (see Fig. 9), we have verified multiple functions of the RASI system under a wide temperature range (–40°C to 40°C), such as: the anti-condensation and frost-prevention functions, the system's self-starting and self-operating functions upon power restoration at low temperatures, and the low-temperature resistance of the bakelite material, etc.

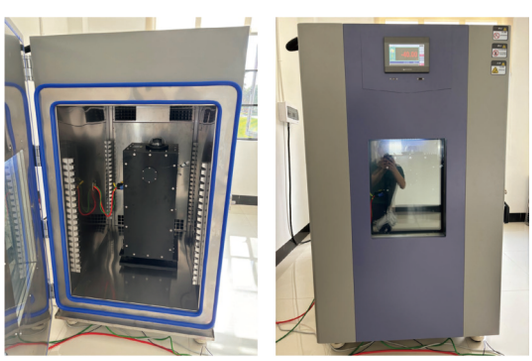


Fig. 9. Robustness test of the RASI system in wide temperature environments.

Through the optimized design of the optical system and the innovative design of the electromechanical system, RASI has been equipped with the hardware conditions for fully automatic observation, but the robotic software control system as described below is also indispensable.

3.3. The Robotic Control System

Several projects for studying the upper atmosphere of the Earth has begun to move towards the stage of networked observation. The MANGO employs twelve ASIs observing the 630.0 nm and 557.7 nm emissions[9]; The Chinese Meridian Project (Ground-besed Space Environment Monitoring Network) established 15 comprehensive stations along the 120°E longitude and 30°N latitude, several dozen ASI devices have been deployed in the stations[38]. The RASIs will perfectly meet the requirements for the networked operation of these projects.

The camera control software of RASI has achieved the ability to conduct scientific observations and data preprocessing independently based on the solar altitude and weather conditions. At the same time, it has also realized the automatic archiving and release capabilities of data.

The robotic control software workflow is shown in Fig. 10. There are three main service threads: Core Main Service (CMS), Task Executor Service (TES) and Data Save Service (DSS). CMS is the main process of the software, it will collect site information (station name, longitude, latitude, altitude, etc) and task requirements (such as: bias task, science data task, etc) by loading the configuration file at first. Then, based on the information of the solar altitude and the all-sky cloud cover, the corresponding observation tasks TES will be autonomously decided to be carried out. The TES process will read various configuration files and start the camera cooling function firstly, then carry out the data collection task secondly, and feed back the execution results to CMS finally. Once the CMS successfully receives the collected image data, it will activate the data storage service thread-DSS. The main function of DSS is to convert the original image data into Flexible Image Transport System (FITS) format and simultaneously generate a compressed image with watermark information, which is convenient for real-time viewing and checking. FITS is the standard archival data format for astronomical data sets. All kinds of information related to data collection can be stored in the FITS file header. That will be beneficial for the image calibration and data processing.

The automatic software can also calculate the solar altitude in real-time by using an astronomical calculation library (libnova[2]), this is conducive to the intelligent execution of the TES and DSS services. Now, let's take the Kjell Henriksen Observatory (78°8.9′N, 16°2.6′E) in Longyearbyen (namely Longyearbyen Station) in the Arctic, and the Lijiang Station (26°41.7′N, 100°1.8′E) of Yunnan Observatories, Chinese Academy of Sciences at a lower latitude as examples, to introduce the changing characteristics of sunrise and sunset throughout everyday in a whole year. When we set the solar altitude at −8° as the

2. *http://libnova.sourceforge.net/*

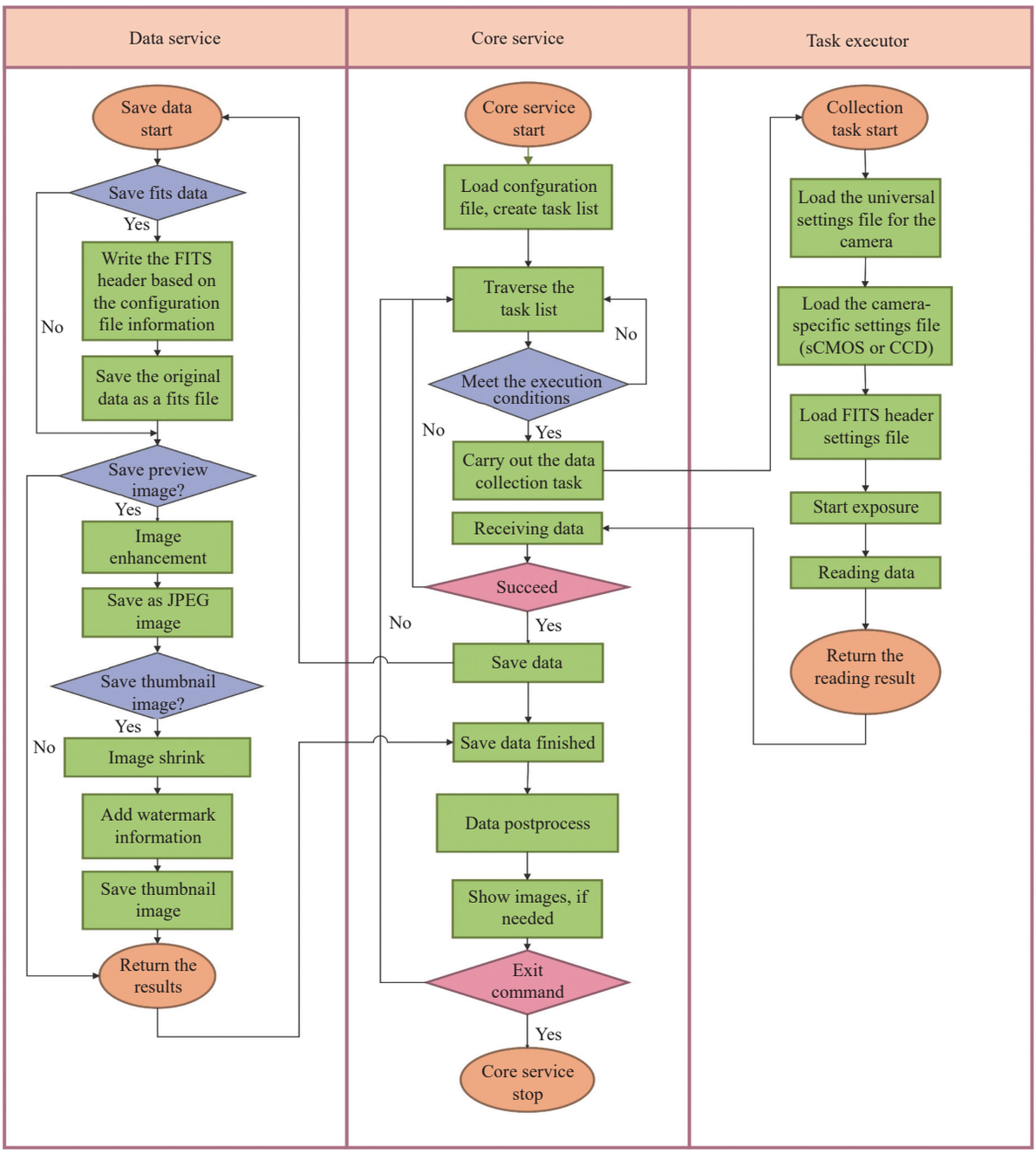


Fig. 10. RASI fully automatic software flow chart.

dividing point between day and night, then we can get the results, which are shown in Fig. 11 and Fig. 12. Obviously, Longyearbyen Station has polar day and polar night, but Lijiang Station does not. Another difference is that the lower the latitude of the site, the longer the observation night-time will be. For example, in the year 2025, Lijiang Station's night-time has 3893.5 h, but Longyearbyen Station's night-time only has 3163.8 h.

In fact, the night sky is not always clear. To avoid the collection of invalid data during the bad nights, RASI achieves the function of automatically collecting data at clear nights, based on the acquisition and judgment of real-time cloud coverage data. The cloud cover data is obtained from the all-sky infrared cloud meter or the all-sky color camera developed by the authors, please refer to the article (Xin et al.[21]) for more details.

The core service also includes a data post-processing section, which mainly involves the operation of merging the bias images and then subtracting the master bias from the scientific data. The dark current values of the cameras are very low (Table 2), which can be ignored.

4. RESULTS AND DISCUSSION

The RASI-1 with Andor EMCCD iXon888 was installed inside a sliding roof at the Lijiang Station since March 2024, and an all-sky color imager is installed not far from RASI-1 since 2018. A sample airglow image

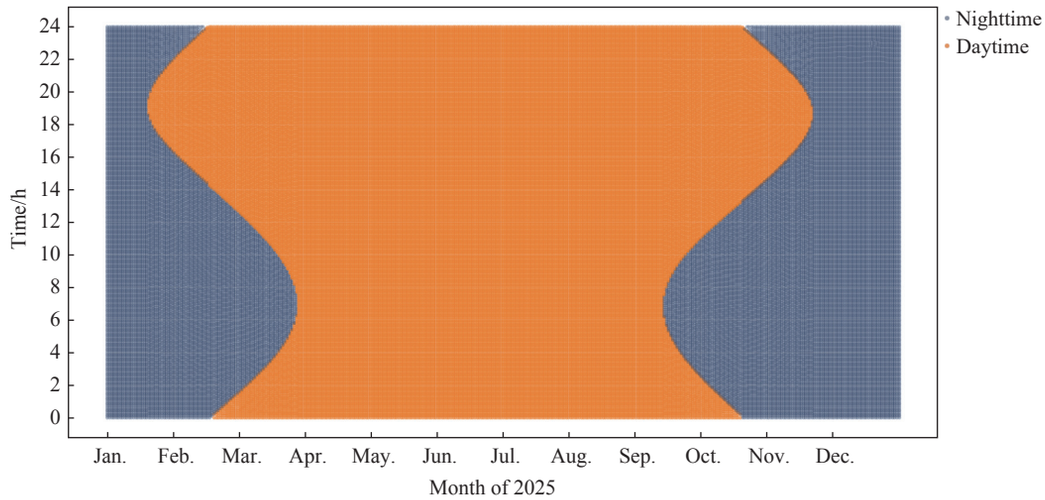


Fig. 11. The times of sunrise and sunset throughout 2025 at Longyearbyen Station.

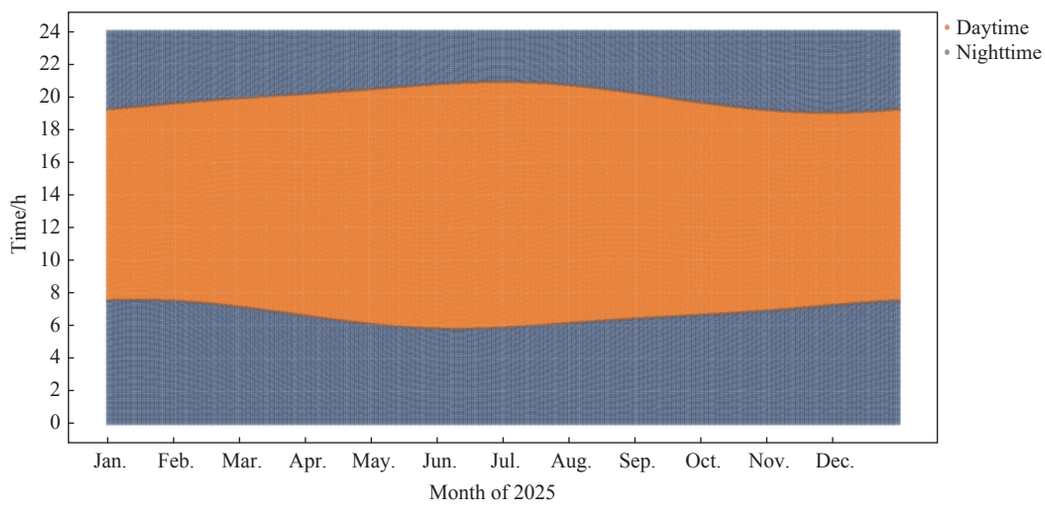


Fig. 12. The times of sunrise and sunset throughout 2025 at Lijiang Station.

taken with a narrow-bandpass filter of 630 nm with 4 s exposure is shown in Fig. 13A. And the color all-sky image captured simultaneously for 59 s exposure is shown in Fig. 13B. The yellow bright line in the color all-sky image comes from the sodium laser guiding star system. As its central wavelength (589 nm) is not within the detection range (630 ± 1.5 nm) of RASI-1, we cannot see it in the narrowband image.

Although a rotation and translation is not applied to the images in Fig 13, the field of view are almost centered with north upwards. In these two images, the Ursa Major constellation in the upper left corner and the Orion constellation in the lower right corner are both very prominent. By comparing color and narrow-band images, the airglow structure is very obvious, and the quality of the starry patterns in narrowband images is also much higher than that in color images. This indicates that the system focus of RASI is excellent, and the image is of good quality, although it is slightly blurred at large zenith angles.

The RASI-2 with Andor EMCCD iXon888 was

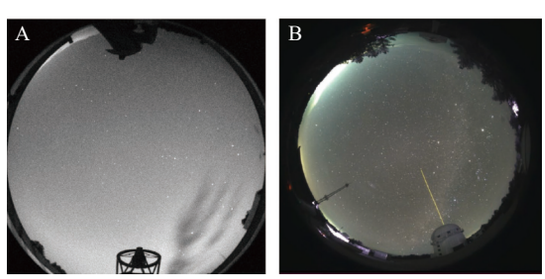


Fig. 13. RASI-1 narrowband gray image (A) and all-sky camera color image (B) at the same time (local time: 2025−05−25 23:50:00) and at the Lijiang Station.

installed on an outdoor platform at Longyearbyen Station since Auguest 2024, and the color all-sky imager was installed simultaneously next to the RASI-2. A sample auroras image taken with a narrow-band filter of 557.7 nm with 4 s exposure is shown in the Fig. 2A. The maximum time resolution of RASI-2 in the continuous acquisition mode is 5 s. The color all-sky image with 20 s exposure is shown in the Fig. 2B. By comparing color and nar-

row-band images, the auroras structure can be clearly displayed in the narrow-band image, but it appears very faint in the color all-sky image. Affected by the moonlight, the blooming effect of the CCD will affect the auroras measurements in certain areas. In order to study the positional and temporal patterns of the auroras or airglow, the image spatial position calibration is necessary. We can obtain the internal and external parameters of the RASI fisheye imaging system by identifying bright stars with known positions across the entire sky. However, simply specifying the temporal-spatial characteristics of auroras or airglow is insufficient, we also need to know the radiation intensity (flux in Rayleighs[39]) to better understand their physical radiation processes. The traditional laboratory flux calibration methods is no longer capable of meeting the precision requirements, Baumgardner et al.[40] proposed an improved method, we have proposed an in-situ calibration method based on the photometric standard stars. All the calibration results will be presented in the next issue of this publication series.

The RASI system still has some limitations. The version of RASI-2 can only conduct robotic measurement for a single narrowband band. If three bands need to be measured simultaneously, three RASI-2 devices are required. Although RASI-1 can achieve multi-band observation by switching the filters through an electrically rotating filter wheel, the focus still needs to be manually adjusted (the next version will be upgraded to electric focusing), so it can only conduct single-narrowband observations.

5. SUMMARY

We developed a new type of standalone RASI with a completely new integrated design of optics, mechanics, and electronics, along with a robotic control system. The new optics utilizes a commercial fisheye lens, a telecentric optical lens, a narrowband filter, the secondary imaging system with focal reducer and a cooled digital CCD camera or sCMOS camera, which provides an all-sky field of view with good image quality and sensitivity. Two version of RASIs (RASI-1 and RASI-2) are developed. RASI-1 has an electric filter wheel and an sCMOS camera, which should be installed in a room with a transparent dome and operate on remote mode. RASI-2 is built as a standalone robotic system with a waterproof and thermal-insulated metal frame housing. Through the adaptive control of the temperature and humidity inside the housing, the transparent hemispherical protective cover has achieved the functions of avoiding condensation and frosting within a wide temperature range. By conducting real-time calculations of the solar altitude and the all-sky cloud cover, RASI-2 can be installed independently outdoors and achieve intelligent and fully automatic observation. Given that compared to CCD detectors, sCMOS detectors have an advantage in the blooming effect, RASI-1 is more suitable for observing the airglows in middle and low latitudes, and RASI-2 is more suitable for observing the auroras in high latitudes.

ACKNOWLEDGEMENTS

We sincerely thank the anonymous referee for constructive comments leading to significant improvement of this paper. The authors acknowledge the projects of the CAS "Light of West China" Program, the National Natural Science Foundation of China (11573067), the Science and Technology Program of Shanghai (21DZ206100), the Ground-based Space Environment Monitoring Network (Chinese Meridian Project II), the Yunnan Revitalization Talent Support Program-Science & Technology Champion Project (202105AB160001) and the Chinese National Antarctic & Arctic Research Expedition for the support of the all-sky auroral/airglow imager program at the Longyearbyen Station and Lijiang Station.

AI DISCLOSURE STATEMENT

AI-assisted technology is not used in the preparation of this work.

AUTHOR CONTRIBUTIONS

Yuxin Xin and Zejun Hu conceived the main ideas, implemented the study, and wrote the paper. Baoli Lun conceived the robotic control system ideas, implemented the study, and wrote the paper. Yue Zhong designed the optical system and implemented the study. Kai Ye and Yuxin Xin designed the electromechanical system ideas and implemented the study. Yuxin Xin and Hongying Xu performed the observations, collected and processed the data. Yufeng Fan, Bin Li and Dehong Huang participated in the installation and testing of RASIs. All authors read and approved the final manuscript.

DECLARATION OF INTERESTS

The authors declare no competing interests.

REFERENCES

[1] Rycroft, M. 1997. Physics of the aurora and airglow. *Journal of Atmospheric and Solar-Terrestrial Physics*, **59** (11): 1359.

[2] Porat, I., Martinez, A., Nguyen, T. V., et al. 2019. All-Sky Imaging for Airglow and Auroral Observations. In Proceedings of AGU Fall Meeting Abstracts.

[3] Singer, S. F. 1957. A new model of magnetic storms and aurorae, Transactions. *American Geophysical Union*, **38**(2): 175−190.

[4] Gonzalez, W. D., Joselyn, J. A., Kamide, Y., et al. 1994. What is a geomagnetic storm? *Journal of Geophysical Research: Space Physics*, **99**(A4): 5771−5792.

[5] Taylor, M. J., Bishop, M. B., Taylor, V. 1995. All-sky

measurements of short period waves imaged in the OI(557.7 nm), Na(589.2 nm) and near infrared OH and O_2(0, 1) nightglow emissions during the ALOHA-93 Campaign. *Geophysical Research Letters*, **22**(20): 2833−2836.

[6] Motoba, T., Kadokura, A., Ebihara, Y., et al. 2008. South Pole all-sky imager observations of dayside aurora activity induced by a solar wind dynamic pressure enhancement. In Prooceedings of AGU Fall Meeting Abstracts.

[7] Nishimura, Y., Lyons, L., Zou, S., et al. 2010. Substorm triggering by new plasma intrusion: THEMIS all-sky imager observations. *Journal of Geophysical Research (Space Physics)*, **115**(A7): A07222.

[8] Deehr, C., Lummerzheim, D. 2001. Ground-based optical observations of hydrogen emission in the auroral substorm. *Journal of Geophysical Research (Space Physics)*, **106**(A1): 33−44.

[9] Bhatt, A. N., Harding, B. J., Makela, J. J., et al. 2023. MANGO: An optical network to study the dynamics of the Earth's upper atmosphere. *Journal of Geophysical Research (Space Physics)*, **128**(10): e2023JA031589.

[10] Miller, S. D., Mills, S. P., Elvidge, C. D., et al. 2012. Suomi satellite brings to light a unique frontier of nighttime environmental sensing capabilities. *Proceedings of the National Academy of Science*, **109**(39): 15706−15711.

[11] Mendillo, M., Baumgardner, J. 1982. Airglow characteristics of equatorial plasma depletions. *Journal of Geophysical Research (Atmospheres)*, **87**(A9): 7641−7652.

[12] Taylor, M. J., Gu, Y. Y., Tao, X., et al. 1995. An investigation of intrinsic gravity wave signatures using coordinated lidar and nightglow image measurements. *Geophysical Research Letters*, **22**(20): 2853−2856.

[13] Medeiros, A. F., Taylor, M. J., Takahashi, H., et al. 2003. An investigation of gravity wave activity in the low-latitude upper mesosphere: Propagation direction and wind filtering. *Journal of Geophysical Research (Atmospheres)*, **108**(D14): 4411.

[14] Otsuka, Y., Shiokawa, K., Ogawa, T., et al. 2004. Geomagnetic conjugate observations of medium-scale traveling ionospheric disturbances at midlatitude using all-sky airglow imagers. *Geophysical Research Letters*, **31**(15): L15803.

[15] Pautet, P. D., Taylor, M. J., Pendleton, W. R., et al. 2014. Advanced mesospheric temperature mapper for high-latitude airglow studies. *Applied Optics*, **53**(26): 5934.

[16] Sarkhel, S., Stober, G., Chau, J. L., et al. 2022. A case study of a ducted gravity wave event over northern Germany using simultaneous airglow imaging and wind-field observations. *Annales Geophysicae*, **40**(2): 179−190.

[17] Krisciunas, K. 1997. Optical night-sky brightness at Mauna Kea over the course of a complete sunspot cycle. *Publications of Astronomical Society of the Pacific*, **109**: 1181−1188.

[18] Walker, D. E., Schwarz, H. E., Bustos, E. 2006. Monitoring the night sky with the Cerro Tololo All-Sky camera for the TMT and LSST projects. In Proceedings of SPIE.

[19] Noll, S., Schmidt, C., Hannawald, P., et al. 2025. PALACE v1.0: Paranal airglow line and continuum emission model. *Geoscientific Model Development*, **18**: 4353−4398.

[20] Castro-Tirado, A. J., Jelínek, M., Vítek, S., et al. 2008. A very sensitive all-sky CCD camera for continuous recording of the night sky. In Proceedings of SPIE.

[21] Xin, Y. X., Bai, J. M., Lun, B. L., et al. 2020. Astronomical site monitoring system at Lijiang Observatory. *Research in Astronomy & Astrophysics*, **20**(9): 149.

[22] Song, T. F., Liu, Y., Wang, J. X., et al. 2020. Site testing campaign for the Large Optical/infrared Telescope of China: general introduction of the Daocheng site. *Research in Astronomy and Astrophysics*, **20**(6): 085.

[23] Xie, H. W., Zhi, H., Kang, Z., et al. 2025. Photometryfree sky area visibility estimation method for All-sky Camera. *Astronomical Techniques and Instruments*, **2**(1): 52−64.

[24] Bernstein, I. B. 1958. Waves in a Plasma in a magnetic field. *Physical Review*, **109**(1): 10−21.

[25] Roble, R. G., Ridley, E. C. 1994. A thermosphere-ionosphere-mesosphere-electrodynamics general circulation model (time-GCM): Equinox solar cycle minimum simulations (30−500 km). *Geophysical Research Letters*, **21**(6): 417−420.

[26] Mendillo, M., Baumgardner, J., Nottingham, D., et al. 1997. Investigations of thermospheric-ionospheric dynamics with 6300-Å images from the Arecibo Observatory. *Journal of Geophysical Research (Space Physics)*, **102**(A4): 7331−7344.

[27] Amorim, D. C. M., Pimenta, A. A., Bittencourt, J. A., et al. 2011. Long-term study of mediumscale traveling ionospheric disturbances using O I 630 nm all-sky imaging and ionosonde over Brazilian low latitudes. *Journal of Geophysical Research (Space Physics)*, **116**(A6): A06312.

[28] Taguchi, M., Ejiri, M., Tomimatsu, K. 2004. A new all-sky optics for aurora and airglow imaging. *Advances in Polar Upper Atmosphere Research*, **18**: 140−148.

[29] Hu, Z. J., Yang, H., Huang, D., et al. 2009. Synoptic distribution of dayside aurora: Multiple-wavelength all-sky observation at Yellow River Station in Ny-Ålesund, Svalbard. *Journal of Atmospheric and Solar-Terrestrial Physics*, **71**(8/9): 794−804.

[30] Johnson, J. W., Öztürk, D. S., Hampton, D., et al. 2024. Automatic detection and classification of Aurora in THEMIS All-Sky Images. *Journal of Geophysical Research Machine Learning and Computation*, **1**(4): 292.

[31] Chakrabarti, S., Upadhyaya, J., Rathi, R., et al. 2025. Automatic localization and characterization of mid-latitude ionospheric plasma structures from allsky airglow images using deep learning framework. *Advances in Space Research*, **76**(4): 2302−2314.

[32] Mende, S. B., Angelopoulos, V., Frey, H. U., et al. 2007. Determination of substorm onset timing and location using the THEMIS ground based observatories. *Geophysical Research Letters*, **34**(17): 17108.

[33] Kendall, E. A., Grill, M., Gudmundsson, E., et al. 2010. The sondrestrom research facility All-sky Imagers. In Proceedings of AGU Fall Meeting Abstracts.

[34] Nishitani, N., Ruohoniemi, J. M., Lester, M., et al. 2019. Review of the accomplishments of mid-latitude Super Dual

Auroral Radar Network (SuperDARN) HF radars. *Progress in Earth and Planetary Science*, **6**(1): 27.

[35] Jochims-Torres, R., Bastidas, M., Bering, E. A., et al. 2024. A student designed and improved All-Sky Imager. In Proceedings of AGU Fall Meeting Abstracts.

[36] Mende, S. B., Eather, R. H., Aamodt, E. K. 1977. Instrument for the monochromatic observation of all sky auroralimages. *Applied Optics*, **16**(6): 1691−1700.

[37] Hu, Z. J., He, F., Liu, J. J., et al. 2017. Multiwavelength and multi-scale aurora observations at the Chinese Zhongshan Station in Antarctica. *Polar Science*, **14**: 1−8.

[38] Wang, C., Xu, J. Y., Liu, L. B., et al. 2023. Contribution of the Chinese Meridian Project to space environment research: Highlights and perspectives. *Science China Earth Sciences*, **66**(7): 1423−1438.

[39] Hunten, D. M., Roach, F. E., Chamberlain, J. W. 1956. A photometric unit for the airglow and aurora. *Journal of Atmospheric and Terrestrial Physics*, **8**(6): 345−346.

[40] Baumgardner, J., Wroten, J., Semeter, J., et al. 2007. A very bright SAR arc: implications for extreme magnetosphere-ionosphere coupling. *Annales Geophysicae*, **25**(12): 2593−2608.